Measurement Techniques of Common Mode Currents, Voltages, and Impedances in a Flyback Converter for Radiated EMI Diagnosis

Juntao Yao, *Student Member, IEEE*, Shuo Wang, *Fellow, IEEE*, and Hui Zhao, *Member, IEEE*

***Abstract*—For the radiated electromagnetic interference pre-compliance diagnosis in power electronics systems, the measurement of common mode (CM) currents, impedances, and voltages are essentially important. In this article, two measurement issues are first identified in CM current and impedance measurement. The first is the coupling between the cables attached to a power converter and the coaxial cable connected to the measurement equipment. It degrades the measurement accuracy. The second is the coupling between the converter's attached cables and the ac grid. It degrades the repeatability of measurements. To improve the measurement accuracy and repeatability, this article proposes an improved measurement technique to address these two issues. Furthermore, for the measurement of the voltage difference between primary and secondary grounds, this article also identifies two issues. The first is the poor measurement resolution for the low noise voltage in the high-frequency range due to the high magnitude of line-frequency voltages. The second is that the loading effects of the voltage probe can reduce the measurement accuracy. This article proposed a technique to address these two issues. Finally, the proposed measurement techniques were validated on a flyback converter.**

***Index Terms*—Common mode (CM), electromagnetic interference (EMI), flyback converter, power converter, radiated emission.**

I. Introduction

With the development of high power density and high switching frequency power converters, and the applications of wide bandgap devices to power conversions, electromagnetic interference (EMI) is becoming an increasingly serious problem. Power converter products need to comply with the international EMI regulation standards, e.g., EN55022 and CISPR 22, before they are allowed to be sold on the market. Anechoic chambers are essential [1] to the radiated EMI measurement. However, given its high cost and large space requirement, anechoic chambers and spectrum analyzers are usually not available in most power electronics labs. Also even with the anechoic chambers, the measured electric field intensity has limited reference values to the analysis and diagnosis of the common mode (CM) noise generated from the power converters.

For isolated power converters with long attached cables, the CM current along the attached cables can be a predominant contributor to the radiated EMI [2]–[9]. Measuring CM current with an oscilloscope is, therefore, a good way for the radiated EMI diagnosis. The measurement techniques for CM currents, impedances, and voltages are therefore very important.

The parasitic coupling effects between the power converter cables and the probe's coaxial cable of the measurement equipment is insignificant in low-frequency range [3], [10], [11]. In high-frequency range, on the other hand, the couplings become significant because of the reduced parasitic impedance between the power converter cables and the probe coaxial cables [12]. The couplings can induce displacement currents flowing through the probe's coaxial cables causing measurement errors. In order to improve the measurement accuracy and repeatability, the measurement technique needs to be improved.

Similarly, for the measurement of the voltage difference between the primary ground (PGND) and the secondary ground (SGND) of the power converter, in the low-frequency range, it usually has high magnitude, so measurement resolution is not an issue. But in high-frequency range, since the high-frequency voltage has a very small magnitude, the resolution of the oscilloscope is extremely critical. The measurement technique should be improved to measure the low magnitude voltages at high frequencies. Furthermore, the input impedance of the probe needs to be considered because it has loading effects on the measurement of the high-frequency voltage difference between PGND and SGND and has negative impact to the radiated EMI diagnosis.

This article is an improved version based on the conference version [4]. New contributions of this article include the following:

1) improved analysis for the coupling issues in the CM current and impedance measurements;
2) improved analysis for the voltage transformations of a switching transformer through its parasitics;
3) improved analysis on the measurement of the voltage difference between PGND and SGND.

In Sections II and III, this article will identify and analyze the effects of the couplings on the CM current and CM impedance

Manuscript received May 29, 2019; revised October 20, 2019; accepted November 10, 2019. Date of publication December 5, 2019; date of current version December 27, 2019. *(Corresponding author: Juntao Yao.)*

J. Yao is with the Department of Electrical and Computer Engineering, University of Florida, Gainesville, FL 32611 USA (e-mail: juntaoyao@ufl.edu).

S. Wang is with the Department of Electrical and Computer Engineering, University of Florida, Gainesville, FL 32611 USA (e-mail: shuowang@ieee.org).

H. Zhao is with the Department of Engineering—Electrical Engineering Division, University of Cambridge, Cambridge CB2 1TN, U.K. (e-mail: hz352@cam.ac.uk).

Color versions of one or more of the figures in this article are available online at http://ieeexplore.ieee.org.

Digital Object Identifier 10.1109/TEMC.2019.2953925

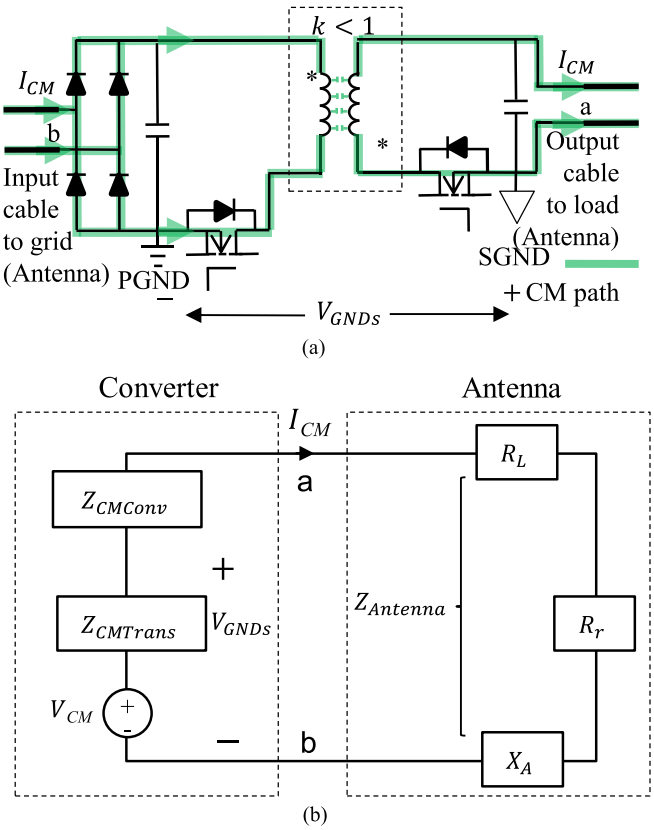

Fig. 1. Converter circuit and CM noise model. (a) Flyback converter with long attached cables. (b) CM noise model.

measurements. An improved measurement technique will be proposed to reduce the coupling effects. Section IV will analyze the issues in the measurement of the voltage difference between PGND and SGND and an improved high-pass filter scheme will be proposed to improve the measurement resolution and to reduce the loading effects of the probe's input impedance. Section V will present experimental verifications for the proposed measurement techniques.

II. CM Current Measurement

A. CM Noise Model of a Flyback Converter

The circuit of a flyback converter with long attached cables and its corresponding CM noise model is shown in Fig. 1. For convenience, other components and circuits in the converter are ignored.

The switching transformer in Fig. 1 is a critical component in the CM noise analysis of a flyback converter. The differential mode (DM) switching voltage caused by the switching on the primary switch can transform to $V_{\rm GNDs}$ across PGND and SGND through the transformer parasitics causing CM current [4], [5], [8], [13] on input and output cables. In Fig. 1(b), the Thevenin equivalence of the transformer and the switching voltage on the primary side is composed of an equivalent CM voltage source $V_{\rm CM}$ and an equivalent impedance $Z_{\rm CMTrans}$. In Fig. 1(b), the CM impedance of the other components such as diode-bridge, PCB traces, etc., on the CM noise propagation path can be characterized with a lumped impedance $Z_{\rm CMConv}$. The input and output attached cables can be characterized with an antenna impedance $Z_{\rm Antenna}$, which is composed of resistance R_L representing cables' power loss, resistance R_r representing cables' radiated power, and reactance X_A representing the near field energy of the cables [14].

According to the CM noise model in Fig. 1(b), the CM current $I_{\rm CM}$ on the cables is given by

$$I_{\rm CM} = \frac{V_{\rm CM}}{Z_{\rm CMTrans} + Z_{\rm CMConv} + Z_{\rm Antenna}} = \frac{V_{\rm GNDs}}{Z_{\rm CMConv} + Z_{\rm Antenna}}. \quad (1)$$

B. Coupling Issues in CM Current Measurement

CM current on cables is measured using a current clamp probe, as shown in Fig. 2(a). Z_g is the grid impedance and V_g is the equivalent grid voltage source. There are two parasitic coupling issues. First, there are the parasitic couplings between input/output cables and the outer conductor (shielding) of the coaxial cable of the current clamp probe. The couplings can be represented with the lumped parasitic coupling impedances $Z_{{\rm CP}i}$ and $Z_{{\rm CP}o}$, as shown in Fig. 2(a). $Z_{{\rm CP}i}$ and $Z_{{\rm CP}o}$, can be extracted using *S*-parameters [15]–[18], [23]. As an example, to extract $Z_{{\rm CP}o}$, a two-port *S*-parameter matrix is first measured between the output cable and the outer conductor of the coaxial cable of the current probe using the setup in Fig. 2(b).

Based on the network theory, the measured *S*-parameter matrix can be converted to impedance matrix and based on the impedance matrix, a π impedance network can be derived in Fig. 2(c). In Fig. 2(c), Z_1 represents the coupling impedance $Z_{{\rm CP}o}$ between two ports. Z_2 and Z_3 are the equivalent impedances to the ground so they are not part of $Z_{{\rm CP}o}$. Based on the network theory, $Z_{{\rm CP}o} = Z_1$ is as follows:

$$Z_{{\rm CP}o} = 2Z_0 \frac{S_{11}S_{22} - (1 - S_{12})(1 - S_{21})}{S_{12}S_{21} - (1 - S_{11})(1 - S_{22})} \quad (2)$$

where S_{11} and S_{22} are reflection coefficients and S_{12} and S_{21} are transmission coefficients.

Similarly, $Z_{{\rm CP}i}$ can also be extracted. The extracted impedances are shown in Fig. 2(d). It is shown that the impedances are from 70 Ω to 1.6 kΩ in the concerned frequency range from 30 to 100 MHz. The CM current can, therefore, flow through parasitic coupling impedances to the coaxial cable of the current clamp probe and cause measurement inaccuracy as analyzed in later sections.

The second parasitic coupling is the CM current path from input cable, to Z_g of the AC grid, to the ground and back to the output cable, as shown in Fig. 2(a). This CM current path can also degrade the measurement accuracy and repeatability for radiated EMI.

C. Techniques to Reduce the Negative Effect of Couplings

For the first parasitic coupling, Fig. 3 shows the equivalent circuit for analysis. $R_{\rm in} = 50\ \Omega$ is the input resistance of the measurement equipment. $Z_{CT{\rm out}} = 5\ \mu$H||30 pF is the output

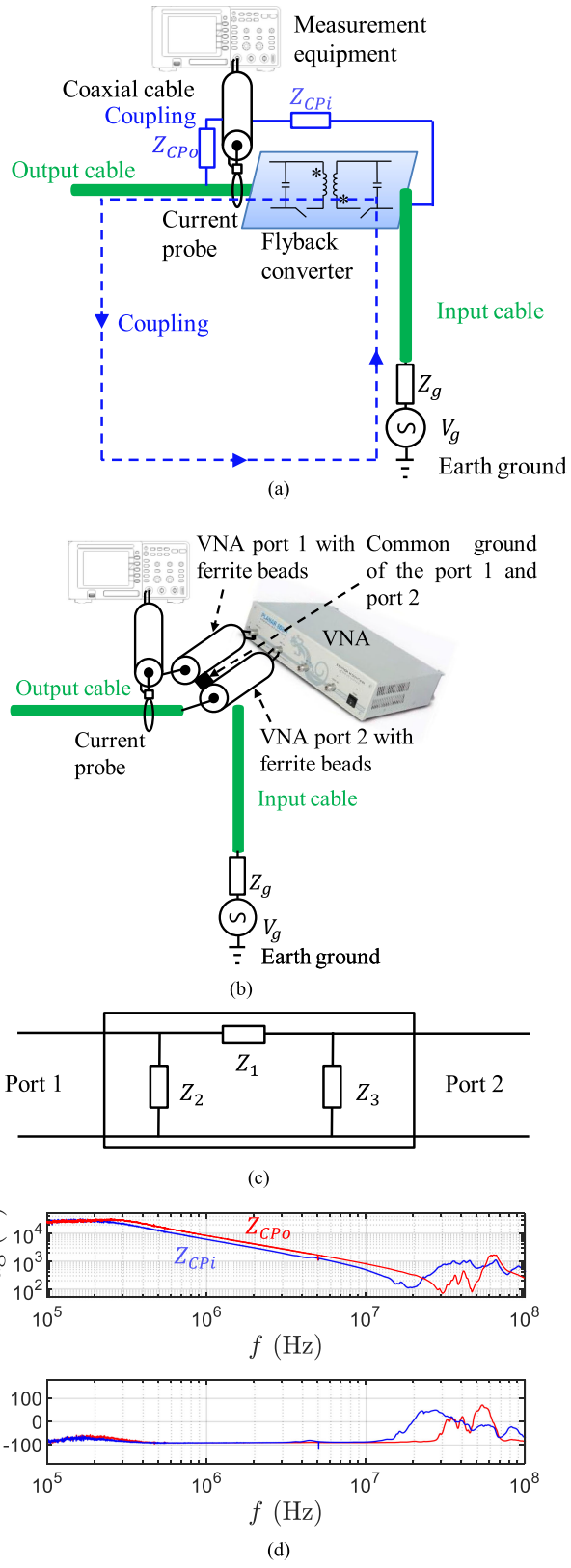

Fig. 2. CM current measurement setup and parasitic coupling extraction. (a) CM current measurement setup with parasitic couplings. (b) *S*-parameter measurement for the coupling extraction. (c) Extracted π network. (d) Extracted parasitic coupling impedances.

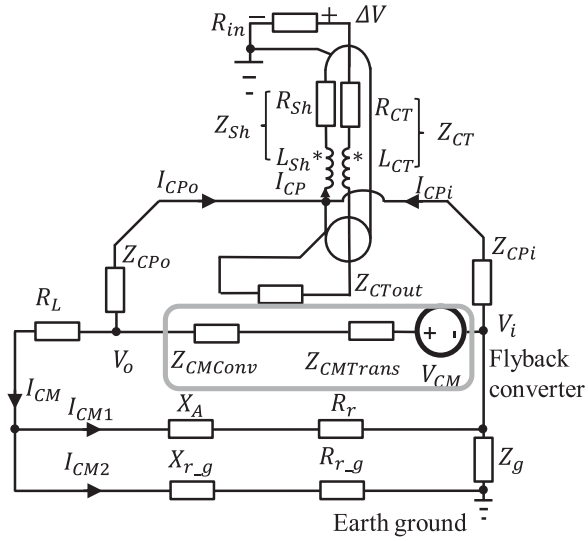

Fig. 3. Equivalent circuit to analyze the CM current measurement with parasitic coupling issues.

impedance of the current clamp probe R&S EZ-17 model 03. X_{r_g} and R_{r_g} represent the reactance and resistance of the coupling loop from the output cable, to ground, to grid impedance and to the input cable as discussed previously. The flyback converter's CM noise model is in the box. The current clamp probe's coaxial cable is modeled with two fully coupled inductances $L_{\rm Sh}$ and L_{CT} and two resistances R_{sh} and R_{CT} for the outer and inner conductors, respectively. The coupling currents I_{CPo} and I_{CPi}, due to the voltage V_o on the output cable, the voltage V_i on the input cable, and the coupling impedances Z_{CPo} and Z_{CPi}, which were measured in Fig. 2, flow to the outer conductor of probe coaxial cable. Due to the full magnetic coupling between the inner and outer conductors of the coaxial cable [19], the induced voltages on two inductances L_{Sh} and L_{CT} cancel each other in the input DM loop of the current probe. The measured error voltage ΔV on $R_{\rm in}$ due to $Z_{\rm CPo}$ and $Z_{\rm CPi}$ is derived based on Fig. 3

This coupling effect can be greatly reduced by adding ferrite beads to the coaxial cable. The ferrite beads should have high resistance in the high-frequency range, so they can greatly increase R_{CT} and R_{Sh}. The ferrite beads will not influence the measured current signal because it is a resistance to CM currents and the measured signal is a DM current in the probe. In the experiments, each ferrite bead Fair-Rite 0431167281 has a resistance 110–330 Ω from 30 to 100 MHz. Ten ferrite beads with a total more than 1.1 kΩ resistance are used. Based on Fig. 3 and (3), shown at the bottom of the the next page, ΔV can be greatly reduced.

For the second parasitic coupling, Fig. 4 shows the equivalent circuit for analysis, where, $Z_{CPg} = jX_{r\_g} + R_{r\_g}$. Due to the uncertainty of the grid impedance, $I_{\rm CM}$ varies at different grid conditions, so measurement is not repeatable. It is, therefore, necessary to reduce the coupling effect between the converter's cables and the ac grid. To solve this, ferrite beads can be used on the cable between the converter's input cable and the power

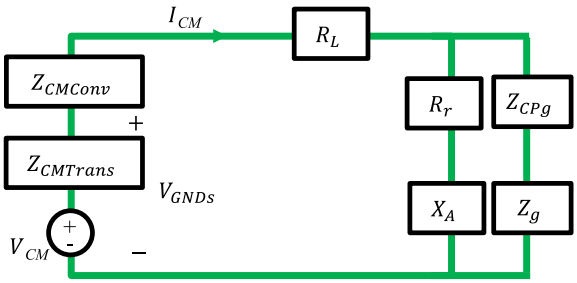

Fig. 4. Equivalent circuit for the parasitic coupling via the ac grid.

grid to increase CM impedance and block the CM current path via the grid.

In summary, to reduce the parasitic coupling between the power converter's input and output cables and the shielding of the current clamp probe's coaxial cable, ferrite beads can be used on the coaxial cable to reduce the CM current flowing to the coaxial cable; to reduce the parasitic coupling between the power cables of the converter via the power grid, the ferrite beads can be used on the cable between the input cable of the power converter and the power grid. Fig. 5(a) shows the implementation of the ferrite beads. Fig. 5(b) shows the comparison of the voltage spectra measured on the oscilloscope with and without the ferrite beads when the current probe is not clamped to the output cable. During the measurement, the converter worked as normal and the ferrite beads are used on the cable between the input cable of the power converter and the power grid. The positions of the current probe, the coaxial cable of the current probe and the converter's cables are the exactly same as those during the normal CM current measurements. Theoretically, the measured voltage should be zero since there is no current flowing through the current clamp. However, as shown in Fig. 5(b), up to 60 dBμV voltage is measured on the oscilloscope. This verified that the coupling is not ignorable. After using ferrite beads, the spectrum is reduced by up to 40 dB, so the ferrite beads greatly help to reduce the undesired coupling to the coaxial cable. Fig. 5(c) shows the measured and the simulated voltage errors ΔV in percentage which is defined as the ratio of the voltage difference between the measured voltages on the oscilloscope without ferrite beads to those with the ferrite beads. It is shown that $Z_{\mathrm{CP}o}$ and $Z_{\mathrm{CP}i}$ can cause significant error.

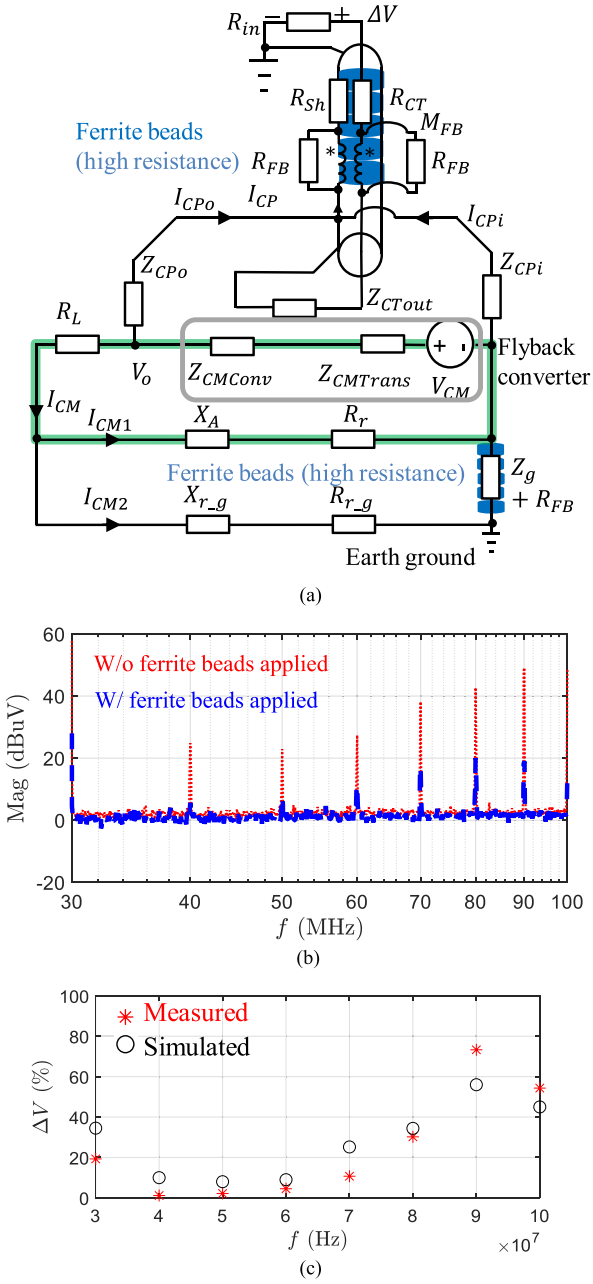

Fig. 5. (a) Using ferrite beads to reduce undesired parasitic couplings. (b) Comparison of the measured voltages with and without the ferrite beads when the current probe is not clamped to the output cable. (c) *Measured* and the simulated voltage errors in percentage when ferrite beads are not used.

III. CM Impedance Measurement

From Fig. 1(b), for the model of the flyback converter, there are three CM impedances, Z_{CMTrans}, Z_{CMConv}, and Z_{Antenna}.

A. Extract Transformer Model

The windings of the transformer in Fig. 1(a) has a nonideal coupling coefficient, so the voltages of primary and secondary windings are not proportional to turns ratio at high frequencies. Furthermore, the transformer is a four-terminal device but its equivalent CM impedance Z_{CMTrans} is a two-terminal impedance, so a technique to convert a four-terminal device to a two-terminal impedance for CM current analysis should be investigated.

$$\Delta V \approx \frac{(Z_{\mathrm{CP}i}V_o + Z_{\mathrm{CP}o}V_i)R_{\mathrm{in}}}{Z_{\mathrm{CP}i}Z_{\mathrm{CP}o}(1+\frac{R_{CT}}{R_{Sh}}+\frac{R_{\mathrm{in}}+Z_{CT\mathrm{out}}}{R_{Sh}}) + (Z_{\mathrm{CP}i}+Z_{\mathrm{CP}o})(R_{CT}+R_{\mathrm{in}}+Z_{CT\mathrm{out}})} \tag{3}$$

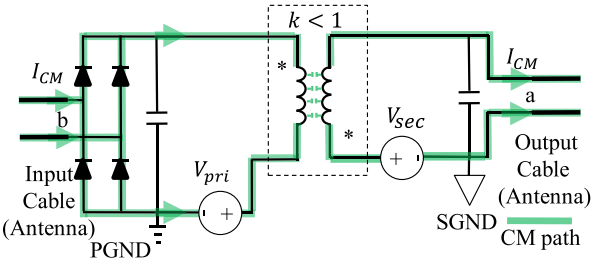

Fig. 6. Using voltage sources to substitute nonlinear switching devices for voltage transformation analysis.

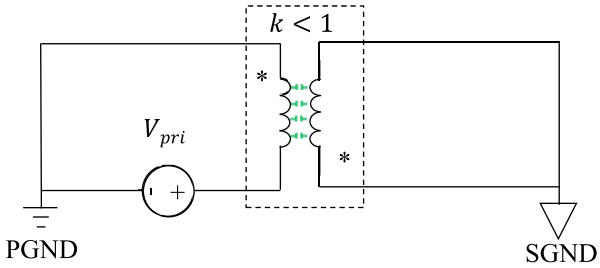

Fig. 7. Transformation from $V_{\rm pri}$ to the voltage across PGND and SGND.

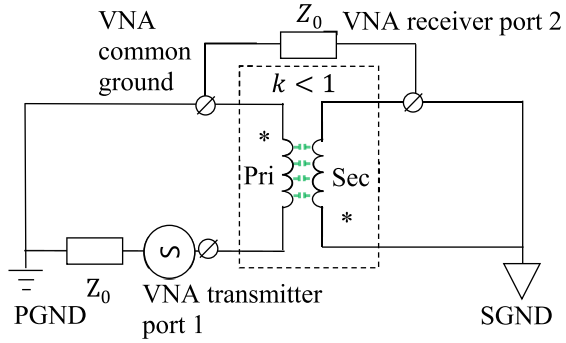

Fig. 8. *S*-parameter measurement to characterize the voltage transformation from $V_{\rm pri}$ to the voltage across PGND and SGND.

In Fig. 1(a), based on substitution theory, both the primary and secondary MOSFETs can be replaced with voltage sources $V_{\rm pri}$ and $V_{\rm sec}$ which have the exact same waveform as those on the MOSFETs to be replaced in Fig. 6. The impedances of the dc bus capacitors on both input and output dc bus can be ignored for EMI analysis so they can be treated as short circuit. Based on the superposition theory, the CM noise generated from $V_{\rm pri}$ and $V_{\rm sec}$ can be analyzed individually by shorting the other voltage source. Fig. 7 shows the analysis of the contribution from $V_{\rm pri}$.

In Fig. 7, $V_{\rm pri}$ is the DM voltage added to the primary winding of the transformer. Due to the parasitic impedances between two windings, this DM voltage can generate $V_{\rm GNDs\_pri}$ across PGND and SGND [20], [21]. The voltage across PGND and SGND is the noise voltage added between the input and output cables. Because of this, there is CM current flowing through the input and output cables which behave like an antenna radiating EMI.

Because the parasitic inductance and capacitance between the two windings are mostly linear, it is possible to find the voltage transformation from $V_{\rm pri}$ to $V_{\rm GNDs\_pri}$ by first measuring *S*-parameter matrix in Fig. 8 and then convert it to voltage

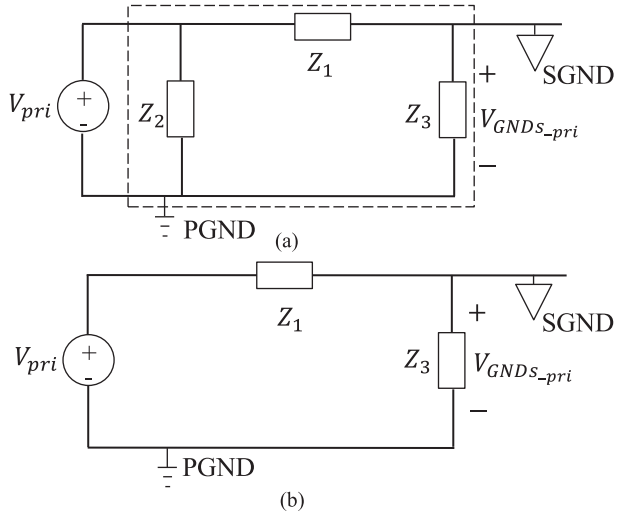

Fig. 9. CM model of the transformer. (a) π model. (b) Reduced model.

gains [17], [25]. In Fig. 8, ports 1 and 2 with input and output impedance Z_o= 50 Ω of a VNA are connected to primary winding and across the PGND and SGND, respectively. It should be pointed out that the setup in Fig. 2(b) is used to extract parasitic coupling impedances, whereas the setup in Fig. 8 is used to extract the circuit model of the transformer.

Based on the measured *S*-parameter matrix, a lumped π impedance model [17], [25] Z_1, Z_2, and Z_3 can be derived in Fig. 9(a). $V_{\rm GNDs\_pri}$ is the voltage on Z_3. Because Z_2 is in parallel with $V_{\rm pri}$, it can be removed. The transformer model can be further reduced to Fig. 9(b).

From Fig. 9(b), the CM transformation gain ($\rm CMTG_{pri}$) from $V_{\rm pri}$ to $V_{\rm GNDs\_pri}$ can be derived as

$$CMTG_{\rm pri} = \frac{V_{GNDs\_pri}}{V_{\rm pri}} = \frac{Z_3}{Z_1 + Z_3}. \tag{4}$$

Similarly, the transformation $\rm CMTG_{sec}$ from $V_{\rm sec}$ to the $V_{\rm GNDs\_sec}$ can be analyzed and measured in Fig. 10(a) and (b).

The total $\rm V_{GNDs}$ across the PGND and SGND is

$$V_{\rm GNDs} = V_{\rm pri} \cdot {\rm CMTG_{pri}} + V_{\rm sec} \cdot {\rm CMTG_{sec}}. \tag{5}$$

Although both $V_{\rm pri}$ and $V_{\rm sec}$ contribute to the voltage $V_{\rm GNDs}$ across the PGND and SGND in (5), due to the magnitude difference between $V_{\rm pri} \cdot {\rm CMTG_{pri}}$ and $V_{\rm sec} \cdot {\rm CMTG_{sec}}$, one could be dominant. Fig. 11 shows the $V_{\rm pri} \cdot {\rm CMTG_{pri}}$ and $V_{\rm sec} \cdot {\rm CMTG_{sec}}$ based on the measured $V_{\rm pri}$, $V_{\rm sec}$, $\rm CMTG_{pri}$, and $\rm CMTG_{sec}$. It is shown that for the flyback converter under investigation, $V_{\rm pri} \cdot CMTG_{\rm pri}$ is dominant in the whole concerned frequency range from 30 to 100 MHz.

Because of this, based on Thevenin equivalence, Fig. 9(b) can be represented with (6) and (7) and Fig. 12.

$$Z_{\rm CMTrans} = Z_1 \| Z_3 \tag{6}$$

$$V_{\rm CM} = V_{\rm pri} \cdot \frac{Z_3}{Z_1 + Z_3} \tag{7}$$

By the way, if both $V_{\rm pri} \cdot {\rm CMTG_{pri}}$ and $V_{\rm sec} \cdot {\rm CMTG_{sec}}$ significantly contribute to the voltage $V_{\rm GNDs}$ across the PGND

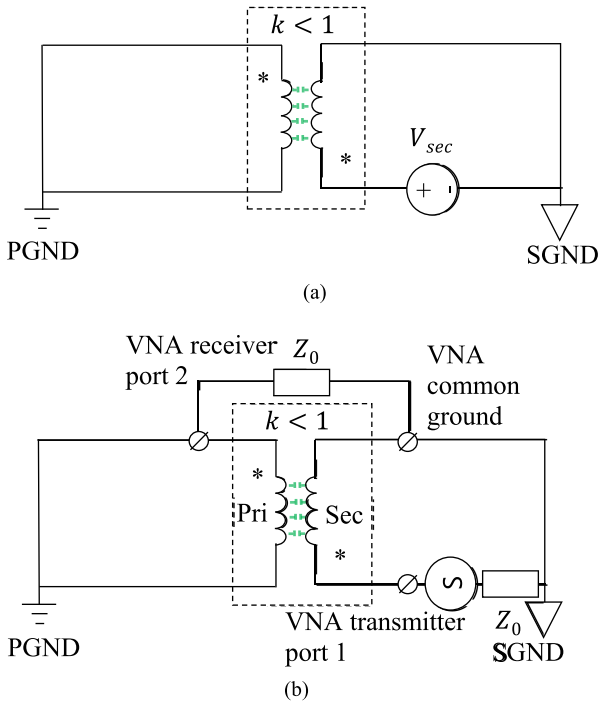

Fig. 10. Characterization of the voltage transformation from $V_{\rm sec}$ to the voltage across PGND and SGND. (a) Voltage transformation from $V_{\rm sec}$. (b) S-parameter measurement to characterize the voltage transformation from $V_{\rm sec}$.

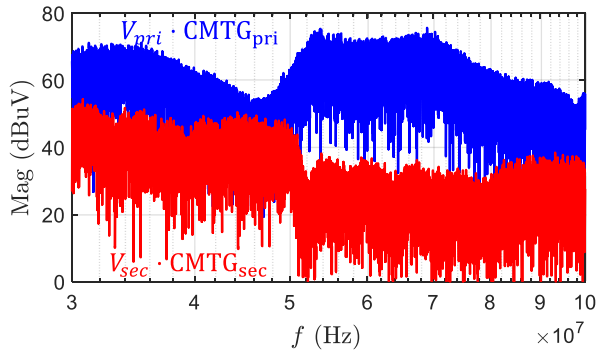

Fig. 11. Voltage across PGND and SGND transformed from the primary and from the secondary sides.

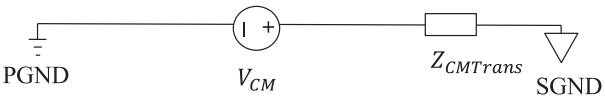

Fig. 12. CM Thevenin equivalence of the transformer and switching voltages.

and SGND, (5) should be used to derive transformer's Thevenin equivalence model.

B. Extract $Z_{\rm CMConv} + Z_{\rm Antenna}$

The total CM impedance of $Z_{\rm CMConv} + Z_{\rm Antenna}$ in Fig. 1(b) can be measured as shown in Fig. 13 after the transformer has been removed from the converter circuit. $Z_{\rm CMConv} + Z_{\rm Antenna}$ can be extracted using the two-port S-parameter as used in Fig. 2.

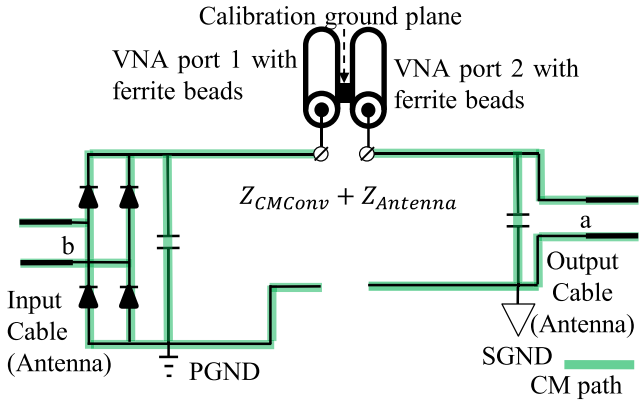

Fig. 13. Measurement setup for $Z_{\rm CMConv} + Z_{\rm Antenna}$.

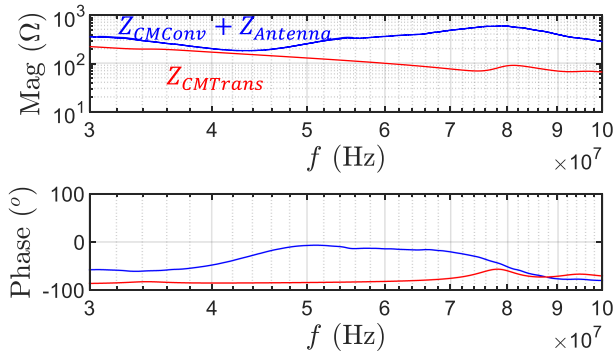

Fig. 14. Impedance comparison of $Z_{\rm CMTrans}$ and $Z_{\rm CMConv} + Z_{\rm Antenna}$.

The impedance can also be measured after shorting the two terminals of the primary as well as the two terminals of the secondary but the result is the same as that in Fig. 13 because of the small impedances of two dc bus capacitors.

Fig. 14 shows the extracted $Z_{\rm CMTrans}$ and the measured $Z_{\rm CMConv} + Z_{\rm Antenna}$. The comparison indicates that $Z_{\rm CMTrans}$ is smaller than $Z_{\rm CMConv} + Z_{\rm Antenna}$. It is, therefore, concluded that although the transformer is a critical component for $V_{\rm CM}$ which finally drives the cables for the radiation, its CM impedance is a minor factor for the radiated EMI. This is especially true for compact transformers with big interwinding parasitic capacitances and small CM impedances.

IV. Measurement of Voltage Across PGND and SGND

The voltage $V_{\rm GNDs}$ across PGND and SGND drives $Z_{\rm CMConv} + Z_{\rm Antenna}$ to generate the CM current and the radiated EMI. However, it also includes line-frequency 50 Hz/60 Hz voltage component. It was shown in Fig. 9(b) that the transformer can be modeled with two impedances across the primary and secondary sides. At low frequencies, these two impedances are mostly capacitance [20], [21] and the total of these two capacitances is equal to the total capacitance, which was measured as 24 pF, between the primary and the secondary windings of the transformer. Thevenin equivalent impedance $Z_{\rm CMTrans}$ in Fig. 12 is, therefore, two capacitances in parallel with a total of 24 pF. There is also a parasitic capacitance between

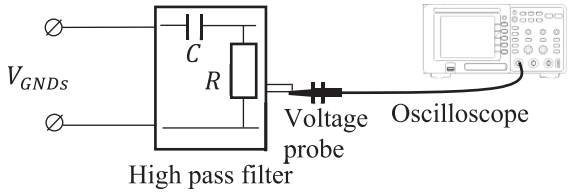

Fig. 15. Conventional approach: a high-pass filter is implemented to block line-frequency voltage for V_{GNDs} measurement.

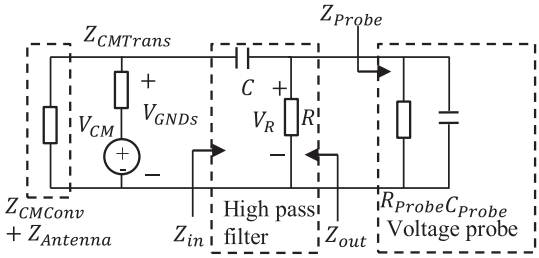

Fig. 16. Equivalent circuit for V_{GNDs} measurement with a high pass filter between V_{GNDs} and the voltage probe.

the output dc bus, output cable and the earth ground. It was measured as 7 pF. Because the operating of the diode bridge, the dc bus on the primary side has a 50 Hz/60 Hz voltage referenced to the earth ground. Because Z_{CMTrans}, which is equal to 24 pF at low frequencies, is in series with the 7 pF parasitic capacitance between the output cable and the ground, there is a 50 Hz/60 Hz voltage drop between PGND and SGND. Depending on the values of ac voltage and parasitic capacitances, this voltage drop could be much bigger than the magnitudes of the high-frequency switching harmonics. For example, if the input voltage is 240 V/ac, with the capacitance above, V_{GNDs} will have a 77 V 50 Hz/60 Hz peak voltage. The oscilloscope cannot easily differentiate high-frequency voltage with small magnitude, for example several mV, from the 50 Hz/60 Hz voltage with a big magnitude. For example, an oscilloscope with 8 digits data resolution has a resolution as poor as 0.625 V at 20 V/div scale. So, it cannot accurately measure mV level V_{GNDs} and cannot catch the noise information in a full line cycle.

A. *Conventional Approach*

Conventionally, an RC high-pass filter is used in Fig. 15 between V_{GNDs} and the voltage probe to block 50 Hz/60 Hz voltage. The RC high-pass filter has a slope of 20 $\mathrm{dB/dec}$. To efficiently reduce the 50 Hz/60 Hz voltage, the cutoff frequency f_c of the filter can be chosen 5 dec higher than the line frequency. It is 5 MHz or 6 MHz.

If the high-pass filter is connected between the V_{GNDs} and the voltage probe as in Fig. 15, the equivalent circuit is shown in Fig. 16. The input impedance Z_{Probe} of the voltage probe is $C_{\mathrm{Probe}}||R_{\mathrm{Probe}}$. The input impedance Z_{in} of the high-pass filter is given as

$$Z_{\mathrm{in}} = R \| Z_{\mathrm{Probe}} + \frac{1}{j2\pi f C}. \tag{8}$$

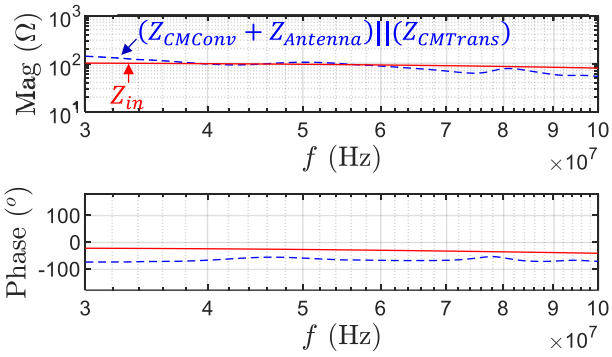

Fig. 17. Comparison of $(Z_{\mathrm{CMConv}} + Z_{\mathrm{Antenna}})||Z_{\mathrm{CMTrans}}$ and Z_{in}.

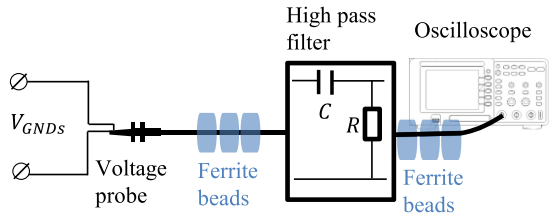

Fig. 18. Improved implementation of the high-pass filter.

Because of the loading effects, the input and output impedances of the high-pass filter must meet conditions (9) and (10) to have accurate measurement results.

$$Z_{\mathrm{in}} \gg (Z_{\mathrm{CMConv}} + Z_{\mathrm{Antenna}}) \| Z_{\mathrm{CMTrans}} \tag{9}$$

$$Z_{\mathrm{out}} \ll Z_{\mathrm{Probe}} \tag{10}$$

For the probe of Rigol RP3500A, $C_{\mathrm{Probe}} = 13$ pF, and $R_{\mathrm{Probe}} = 10$ M Ω. Considering $Z_{\mathrm{out}} = R$ at the worst scenario, based on (10), $R < 112.49$ Ω, so the filter can be designed as$R = 100$ Ω, $C = 300$ pF, with $f_c = 5.3$MHz.

Fig. 17 shows the comparison of the measured Z_{in} and $(Z_{\mathrm{CMConv}} + Z_{\mathrm{Antenna}})||Z_{\mathrm{CMTrans}}$. It indicates that (9) cannot be met, therefore, the high-pass filter cannot meet both (9) and (10) at the same time, so it cannot be used to directly measure V_{GNDs}, as shown in Fig. 16.

B. *Proposed Approach*

To solve this issue, the high-pass filter can be moved to between the voltage probe and the coaxial cable as in Fig. 18.

Similarly, the condition (11) should be met to reduce oscilloscope's loading effect on the voltage probe

$$|Z_{\mathrm{out}}| \ll \left| \frac{1}{j2\pi f C_{\mathrm{OS}} + \frac{1}{R_{\mathrm{OS}}}} \right| \tag{11}$$

where $C_{\mathrm{OS}}||R_{\mathrm{OS}}$ is the input impedance of the oscilloscope. For Rigol MSO4054, $C_{\mathrm{OS}} = 15$ pF, and $R_{\mathrm{OS}} = 1$ MΩ. Similarly, Considering $Z_{\mathrm{out}} = R$ at the worst scenario, based on (15) at 100 MHz, $R < 106.16$ Ω. Also, the output impedance of the voltage probe is a 195 pF capacitance and it has an impedance

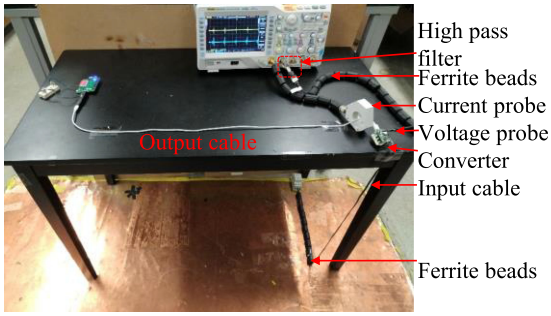

Fig. 19. Measurement setup.

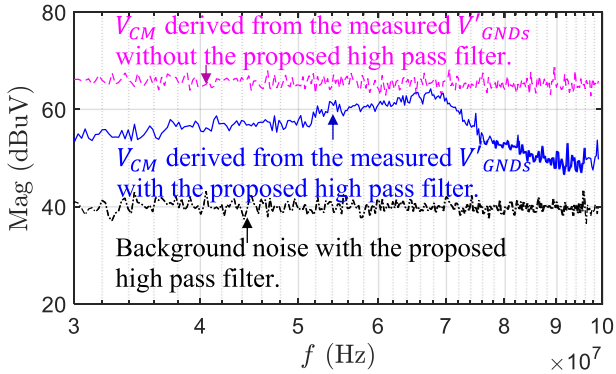

Fig. 20. Spectrum comparison of $V_{\rm CM}$ with and without a proposed high-pass filter and the background noise with the proposed high-pass filter.

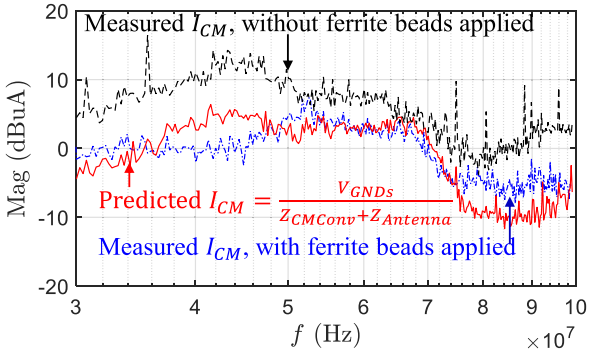

Fig. 21. Comparison of the measured and predicted CM current spectra.

smaller than 27 Ω above 30 MHz, so R should be much larger than 27 Ω. Based on these conditions, the RC filter is designed as$R = 100\ \Omega$, $C = 300$ pF. For the same reason as the current probe, to reduce the parasitic coupling to the coaxial cable of the voltage probe, ferrite beads are used on the coaxial cable before and after the high-pass filter. Furthermore, because the voltage probe has an input impedance of $Z_{\rm Probe} = 13$ pF||1 MΩ, it has a loading effect on the $V_{\rm GNDs}$ measurement as it is equivalently in parallel with $Z_{\rm CMConv} + Z_{\rm Antenna}$. So the directly measured $V_{\rm GNDs}$ is not the actual $V_{\rm GNDs}$ when the voltage probe is not connected between PGND and SGND. To solve this issue, high resistive ferrite beads are used on both input and output cables of the converter to provide high impedance to block the antenna impedance, so the measured $V_{\rm GNDs}$ will be the output of the voltage divider composed of $Z_{\rm CMTrans}$ and $Z_{\rm Probe}$. The $V_{\rm CM}$ and actual $V_{\rm GNDs}$ can, therefore, be derived based on the measured $V'_{\rm GNDs}$ as

$$V_{\rm CM} = V'_{\rm GNDs}\,(1 + Z_{\rm CMTrans}/\,Z_{\rm Probe}) \tag{12}$$

$$V_{\rm GNDs} = V_{\rm CM}\,(\,Z_{\rm CMConv} + Z_{\rm Antenna})\,/\,(\,Z_{\rm CMConv} + Z_{\rm Antenna} + Z_{\rm CMTrans})\,. \tag{13}$$

V. Experimental Verification

Fig. 19 shows the measurement setup based on the proposed measurement techniques on a flyback converter on a table. The input voltage of the converter is 240 V/60 Hz, the output is 5 V/4.5 A. The switching frequency is 65 kHz. The output cable is a 0.9 m USB-A to USB type-C cable with a load adapter and a 1.1 Ω load resistor. The height of the table is 0.8 m. The input cable is perpendicular to the ground as shown in the figure. High-frequency resistive ferrite beads (Fair-Rite 0431167281) are used on the coaxial cables of the current clamp probe and the voltage probe. The ferrite beads are also used on the cable on the ground between the input cable of the flyback converter and the ac grid. The oscilloscope is Rigol MSO4054. The current probe is EZ-17 Model03 from Rohde & Schwarz and the voltage probe is Rigol RA3500A. In S-parameter measurement, the VNA is Planar 808/1 from Copper Mountain.

Fig. 20 shows the spectrum comparison of the $V_{\rm CM}$ derived from the measured $V'_{\rm GNDs}$ based on the measured time domain waveforms with and without using the proposed high-pass filter. The background noise with the proposed high-pass filter when the converter is turned OFF is also measured in Fig. 20.

It is shown that without using the proposed high-pass filter technique, because the resolution of the oscilloscope is not enough for high-frequency low magnitude voltage measurement, the whole spectrum shows high noise floor in Fig. 20. On the other hand, the background noise with the proposed high-pass filter is much smaller than the derived $V_{\rm CM}$. Because of this, the proposed high-pass filter improved the signal-to-noise ratio.

With the $V_{\rm GNDs}$ and $Z_{\rm CMConv} + Z_{\rm Antenna}$, the CM current on the input and output cables can be predicted based on Fig. 4, as shown in Fig. 21. On the other hand, based on the directly measured CM current time-domain waveforms, the spectrum of the CM current is also derived in the figure. The dashed black curve is the CM current spectrum derived from the directly measured time-domain waveform of the CM current without using any ferrite beads. In Fig. 21, the difference between the predicted and the measured CM current spectra is less than 6 dB. Therefore, the proposed techniques for CM current, impedance, and voltage measurement are verified. It should be pointed out that the measured CM currents on input and output cable are almost the same. The CM current is also almost constant along the cables. The spectrum of the measured CM current without using any ferrite beads much deviates from the accurate value, so it is incorrect.

VI. Conclusion

In this article, several measurement techniques are proposed for CM current, voltage, and impedance measurement for radiated EMI analysis. The coupling between the coaxial cable of a current probe and the input and output cables of a flyback converter is analyzed. The model is developed and a technical solution is proposed. The CM model of a switching transformer is developed and its voltage transformations from the DM voltages to the voltage across PGND and SGND and its impedances are extracted based on measurements. A high-pass filter implementation for measuring the voltage across PGND and SGND is proposed. The proposed techniques are finally validated in experiments.

References

[1] *American National Standard for Methods of Measurement of Radio-Noise Emissions from Low-Voltage Electrical and Electronic Equipment in the Range of 9 kHz to 40 GHz*, ANSI C63.4-2014 (Revision of ANSI C63.4-2009), pp. 1–170, 2014.

[2] D. M. Hockanson, J. L. Drewniak, T. H. Hubing, T. P. V. Doren, S. Fei, and M. J. Wilhelm, "Investigation of fundamental EMI source mechanisms driving common-mode radiation from printed circuit boards with attached cables," *IEEE Trans. Electromagn. Compat.*, vol. 38, no. 4, pp. 557–566, Nov. 1996.

[3] M. Laour, R. Tahmi, and C. Vollaire, "Modeling and analysis of conducted and radiated emissions due to common mode current of a buck converter," *IEEE Trans. Electromagn. Compat.*, vol. 59, no. 4, pp. 1260–1267, Aug. 2017.

[4] J. Yao *et al.*, "Measurement techniques of CM currents, impedance and voltages for radiated EMI in isolated power converters," in *Proc. IEEE Symp. Electromagn. Compat., Signal Integr. Power Integr.*, 2018, pp. 438–443.

[5] J. Yao *et al.*, "Modeling and reduction of radiated common mode current in flyback converters," in *Proc. IEEE Energy Convers. Congr. Expo.*, 2018, pp. 6613–6620.

[6] J. Jia, D. Rinas, and S. Frei, "Predicting the radiated emissions of automotive systems according to CISPR 25 using current scan methods," *IEEE Trans. Electromagn. Compat.*, vol. 58, no. 2, pp. 409–418, Apr. 2016.

[7] Y. Huangfu, S. Wang, L. D. Rienzo, and J. Zhu, "Radiated EMI modeling and performance analysis of a PWM PMSM drive system based on field-circuit coupled FEM," *IEEE Trans. Magn.*, vol. 53, no. 11, Nov. 2017, Art. no. 8208804.

[8] Y. Zhang, S. Wang, and Y. Chu, "Investigation of radiated electromagnetic interference for an isolated high frequency DC-DC power converter with power cables," *IEEE Trans. Power Electron.*, vol. 34, no. 10, pp. 9632–9643, Oct. 2019.

[9] C. R. Paul, "A comparison of the contributions of common-mode and differential-mode currents in radiated emissions," *IEEE Trans. Electromagn. Compat.*, vol. 31, no. 2, pp. 189–193, May 1989.

[10] H. Chen, Y. Yan, and H. Zhao, "Extraction of common-mode impedance of an inverter-fed induction motor," *IEEE Trans. Electromagn. Compat.*, vol. 58, no. 2, pp. 599–606, Apr. 2016.

[11] Y. Liu, K. Y. See, S. Yin, R. Simanjorang, A. K. Gupta, and J. Lai, "Equivalent circuit model of high power density SiC converter for common-mode conducted emission prediction and analysis," *IEEE Electromagn. Compat. Mag.*, vol. 8, no. 1, pp. 67–74, Jan.–Mar. 2019.

[12] Z. Vrankovic, G. L. Skibinski, and C. Winterhalter, "Novel double clamp methodology to reduce shielded cable radiated emissions initiated by electronic device switching," *IEEE Trans. Ind. Appl.*, vol. 53, no. 1, pp. 327–339, Jan./Feb. 2017.

[13] Y. Li, S. Wang, H. Sheng, S. Lakshmikanthan, and C. P. Chng, "Investigation and reduction of line frequency common mode voltages at the outputs of AC/DC power converters," in *Proc. IEEE Int. Symp. Electromagn. Compat. Signal/Power Integr.*, 2017, pp. 364–369.

[14] C. Balanis, *Antenna Theory: Analysis and Design*. Hoboken, NJ, USA: Wiley Blackwell, 2016.

[15] Y. Zhang, S. Wang, and Y. Chu, "Modeling and reduction of radiated EMI for isolated power converters," in *Proc. IEEE Appl. Power Electron. Conf. Expo.*, 2018, pp. 1778–1785.

[16] R. Meys and F. Janssens, "Measuring the impedance of balanced antennas by an S-parameter method," *IEEE Antennas Propag. Mag.*, vol. 40, no. 6, pp. 62–65, Dec. 1998.

[17] S. Wang, F. C. Lee, and W. G. Odendaal, "Characterization and parasitic extraction of EMI filters using scattering parameters," *IEEE Trans. Power Electron.*, vol. 20, no. 2, pp. 502–510, Mar. 2005.

[18] S. Wang, F. C. Lee, D. Y. Chen, and W. G. Odendaal, "Effects of parasitic parameters on EMI filter performance," in *IEEE Trans. Power Electron.*, vol. 19, no. 3, pp. 869–877, May 2004.

[19] H. Ott, *Noise Reduction Techniques in Electronic Systems*. New York, N.Y.: Wiley, 1988.

[20] H. Zhang, S. Wang, Y. M. Li, Q. H. Wang, and D. B. Fu, "Two-capacitor transformer winding capacitance models for common-mode EMI noise analysis in isolated DC-DC converters," *IEEE Trans. Power Electron.*, vol. 32, no. 11, pp. 8458–8469, Nov 2017.

[21] Y. Li, H. Zhang, S. Wang, H. Sheng, C. P. Chng, and S. Lakshmikanthan, "Investigating switching transformers for common mode EMI reduction to remove common mode EMI filters and Y capacitors in flyback converters," *IEEE J. Emerg. Sel. Topics Power Electron.*, vol. 6, no. 4, pp. 2287–2301, Dec. 2018.

[22] S. Wang, F. C. Lee, and W. G. Odendaal, "Single layer iron powder core inductor model and its effect on boost PFC EMI noise," in *Proc. IEEE 34th Annu. Conf. Power Electron. Spec.*, 2003, vol. 2, pp. 847–852.

[23] S. Wang, F. C. Lee, and W. G. Odendaal, "Using scattering parameters to characterize EMI filters," in *Proc. IEEE 35th Annu. Power Electron. Spec.*, Aachen, Germany, 2004, vol. 1, pp. 297–303.

[24] H. Zhao, J. Yao, and S. Wang, "A universal DM/CM physical model for power transformer EMI analysis within both conducted and radiated frequency ranges," in *Proc. IEEE Energy Convers. Congr. Expo.*, Portland, OR, USA, 2018, pp. 6592–6599.

[25] D. A. Frickey, "Conversions between S, Z, Y, H, ABCD, and T parameters which are valid for complex source and load impedances," *IEEE Trans. Microw. Theory Techn.*, vol. 42, no. 2, pp. 205–211, Feb. 1994.

Juntao Yao (S'15) received the B.S. and M.S. degrees in electrical engineering from Wuhan University, Wuhan, China, in 2013 and 2016, respectively. He is currently working toward the Ph.D. degree with the University of Florida, Gainesville, FL, USA.

His research interests include power electronics, electromagnetic interference, and magnetic components.

Shuo Wang (S'03–M'06–SM'07–F'19) received the Ph.D. degree in electrical engineering from Virginia Tech, Blacksburg, VA, USA, in 2005.

He is currently a Full Professor with the Department of Electrical and Computer Engineering, University of Florida, Gainesville, FL, USA. He has authored/coauthored more than 180 IEEE journal and conference papers and holds around 30 pending/issued US/international patents.

Dr. Wang was a recipient of the Best Transaction Paper Award from the IEEE Power Electronics Society in 2006, two William M. Portnoy Awards for the papers published in the IEEE Industry Applications Society in 2004 and 2012, respectively, and the prestigious National Science Foundation CAREER Award in 2012. He is an Associate Editor for the IEEE Transactions on Industry Applications and a Technical Program Co-Chair for the IEEE 2014 International Electric Vehicle Conference.

Hui Zhao (S'14–M'18) received the bachelor's and master's degrees in electrical engineering from the Huazhong University of Science and Technology, Wuhan, China, in 2010 and 2013, respectively, and the Ph.D. degree in power electronics from the University of Florida, Gainesville, FL, USA, in 2018.

He had a Summer Internship with General Electric Global Research Center, Shanghai, China, in 2013. He is currently a Postdoctoral Research Associate with the University of Cambridge, Cambridge, U.K. His research interests include the modeling and driving of the power devices, EMI, and high power density power converters.